

# Physical properties of asteroid Dimorphos as derived from the DART impact

S.D. Raducan<sup>\*1</sup>, M. Jutzi<sup>1</sup>, A.F. Cheng<sup>2</sup>, Y. Zhang<sup>3</sup>, O. Barnouin<sup>2</sup>, G. S. Collins<sup>4</sup>, R. T. Daly<sup>2</sup>, T. M. Davison<sup>4</sup>, C.M. Ernst<sup>2</sup>, T. L. Farnham<sup>3</sup>, F. Ferrari<sup>5</sup>, M. Hirabayashi<sup>6,7</sup>, K. M. Kumamoto<sup>8</sup>, P. Michel<sup>9,10</sup>, N. Murdoch<sup>11</sup>, R. Nakano<sup>6,7</sup>, M. Pajola<sup>12</sup>, A. Rossi<sup>13</sup>, H. F. Agrusa<sup>9,3</sup>, B. W. Barbee<sup>14</sup>, M. Bruck Syal<sup>8</sup>, N. L. Chabot<sup>2</sup>, E. Dotto<sup>15</sup>, E. G. Fahnestock<sup>16</sup>, P. H. Hasselmann<sup>15</sup>, I. Herreros<sup>17</sup>, S. Ivanovski<sup>18</sup>, J.-Y. Li<sup>19</sup>, A. Lucchetti<sup>12</sup>, R. Luther<sup>20</sup>, J. Ormö<sup>17</sup>, M. Owen<sup>8</sup>, P. Pravec<sup>21</sup>, A. S. Rivkin<sup>2</sup>, C. Q. Robin<sup>11</sup>, P. Sánchez<sup>22</sup>, F. Tusberti<sup>12</sup>, K. Wünnemann<sup>20</sup>, A. Zinzi<sup>23</sup>, E. Mazzotta Epifani<sup>15</sup>, C. Manzoni<sup>24</sup>, and B. H. May<sup>24</sup>

<sup>1</sup>Space Research and Planetary Sciences, Physics Institute, University of Bern, Switzerland

<sup>2</sup>Johns Hopkins University Applied Physics Laboratory, Laurel, MD, USA

<sup>3</sup>Department of Aerospace Engineering, University of Maryland, College Park, MD, USA

<sup>4</sup>Department of Earth Science and Engineering, Imperial College London, UK

<sup>5</sup>Department of Aerospace Science and Technology, Politecnico di Milano, Italy

<sup>6</sup>Guggenheim School of Aerospace Engineering, Georgia Institute of Technology, Atlanta, GA, USA

<sup>7</sup>Department of Aerospace Engineering, Auburn University, Auburn, AL, USA

<sup>8</sup>Lawrence Livermore National Laboratory, Livermore, CA, USA

<sup>9</sup>Université Côte d'Azur, Observatoire de la Côte d'Azur, CNRS, Laboratoire Lagrange, Nice, France

<sup>10</sup>University of Tokyo, Department of Systems Innovation, School of Engineering, Tokyo, Japan

<sup>11</sup>Institut Supérieur de l'Aéronautique et de l'Espace (ISAE-SUPAERO), Université de Toulouse, Toulouse, France

<sup>12</sup>INAF-OAPD Astronomical Observatory of Padova, Italy

<sup>13</sup>IFAC-CNR, Sesto Fiorentino (FI), Italy

<sup>14</sup>NASA/Goddard Space Flight Center, Greenbelt, MD, USA

<sup>15</sup>INAF-Osservatorio Astronomico di Roma, Italy

<sup>16</sup>Jet Propulsion Laboratory, California Institute of Technology, Pasadena, CA, USA

<sup>17</sup>Centro de Astrobiología (CAB), CSIC-INTA, Carretera de Ajalvir km4, 28850 Torrejón de Ardoz, Spain

<sup>18</sup>INAF-Osservatorio Astronomico di Trieste, Trieste, Italy

<sup>19</sup>Planetary Science Institute, Tucson, AZ, USA

<sup>20</sup>Museum für Naturkunde, Leibniz Institute for Evolution and Biodiversity Science, Berlin, Germany

<sup>21</sup>Astronomical Institute of the Czech Academy of Sciences, Czech Republic

<sup>22</sup>Colorado Center for Astrodynamics Research, University of Colorado Boulder, Boulder, CO, USA

<sup>23</sup>Agenzia Spaziale Italiana; ASI Space Science Data Center, Italy

<sup>24</sup>London Stereoscopic Company, London, UK

On September 26, 2022, NASA’s Double Asteroid Redirection Test (DART) mission successfully impacted Dimorphos, the natural satellite of the binary near-Earth asteroid (65803) Didymos. Numerical simulations of the impact provide a means to explore target surface material properties and structures, consistent with the observed momentum deflection efficiency, ejecta cone geometry, and ejected mass. Our simulation, which best matches observations, indicates that Dimorphos is weak, with a cohesive strength of less than a few pascals (Pa), similar to asteroids (162173) Ryugu and (101955) Bennu. We find that a bulk density of Dimorphos,  $\rho_B$ , lower than  $\approx 2400 \text{ kg/m}^3$ , and a low volume fraction of boulders ( $\lesssim 40 \text{ vol}\%$ ) on the surface and in the shallow subsurface, are consistent with measured data from the DART experiment. These findings suggest Dimorphos is a rubble pile that might have formed through rotational mass shedding and re-accumulation from Didymos. Our simulations indicate that the DART impact caused global deformation and resurfacing of Dimorphos. ESA’s upcoming Hera mission may find a re-shaped asteroid, rather than a well-defined crater.

## Introduction

DART was a planetary defense mission to demonstrate the feasibility of using a kinetic impactor to change the trajectory of an asteroid [1]. The impact was successful and highly effective, resulting in a reduction in Dimorphos’ orbital period around Didymos, which was initially 11 hours and 55 minutes, by  $33 \pm 1$  minutes [2]. The LICIACube Unit Key Explorer (LUKE) instrument onboard the cubesat [3] captured images of the system between 29 and 320 seconds after impact, revealing filamentary streams of ejecta and other complex patterns that expanded for several kilometres from the impact site [4]. Moreover, the dramatic brightening of the Didymos system by solar illumination of released impact ejecta was observed from ground- and space-based telescopes [2, 5, 6] for many weeks after the impact.

The obtained 33-minute reduction in the binary orbital period [2] implies a momentum transfer to Dimorphos that exceeded the incident momentum of the DART spacecraft by a factor  $\beta$ , ranging from 2.2 to 4.9, depending on the mass of Dimorphos [7] – which is not currently known but will be measured by the ESA Hera spacecraft in early 2027 [8]. The  $\beta$  parameter is defined as the ratio of the target momentum increment after the impact to the impactor momentum, in the direction of the net ejecta momentum, and is related to the additional thrust from the production of impact ejecta [7, 9].  $\beta$  strongly depends on impact conditions (i.e., impact velocity and impact angle [1]) and target material properties, such as strength, porosity, bulk density and target surface structure [10–12].

The spacecraft information, location and impact angle for the DART impact are well understood [1]. However, the mass and surface properties of Dimorphos are still ambiguous. It was not possible to directly measure the mass and bulk density of Dimorphos with DART or LICIACube. Instead, these parameters were estimated from the total mass of the binary system, derived from Dimorphos’ orbit [13], and updated volume estimates of Didymos and Dimorphos provided by DART [1]. The estimated bulk density of Dimorphos ranges from  $\rho_B = 1500$  to  $3300 \text{ kg/m}^3$  [1, 7].

The surface material properties and sub-surface structure of Dimorphos were also not directly measured. However, these target parameters are vital for understanding the impact process and transforming the kinetic impactor method from a full-scale experiment by DART into a well-understood and reliable mitigation technique for planetary defence. Moreover, knowledge of the material properties of Dimorphos relates to the origin and evolution of the Didymos-Dimorphos system, as well as the overall characteristics of rubble-pile asteroids and binary asteroid systems.

In this work, we simulate the DART impact numerically and compare the results with observations to infer the properties of Dimorphos. We performed numerical simulations of the DART impact using the shock physics code *Bern SPH* [14, 15] over a range of assumed sets of material properties and interior structures for Dimorphos. We represented the DART spacecraft as a low-density spherical projectile of equivalent mass (see Projectile section in Methods), and the impact velocity and angle were also kept fixed. We simulated the asteroid’s response to the DART impact for up to one hour after the time of impact, using the numerical approach developed in [16, 17] to model late-stage, low-speed deformation (see Modelling approach for the late stage evolution in Methods). Bern SPH’s fast-integration scheme was

---

\*sabina.raducan@unibe.ch

validated against laboratory experiments [18] and recently applied successfully to the Hayabusa2 SCI impact modelling [17]. Due to the relatively short timescales modelled, the rotation of Dimorphos around Didymos and Didymos’s gravity were not accounted for.

We obtain realistic configurations of boulders for our rubble-pile targets from simulations of gravitational collapse of a cloud of spherical particles with a predefined size-frequency distribution (SFD) [1, 19]. To closely replicate the topography described by [1], we then selectively removed particles positioned near the surface.

To explore a large possible range of boulder volume fractions (0 vol% to 50 vol%), we replaced some of these boulders with matrix material when we built our target asteroid. We only explicitly modelled boulders larger than 2.5 m in diameter, and the space between boulders was filled with matrix material. Boulders smaller than 2.5 m were removed from the SFD because they were too small to be resolved individually. Thus, components smaller than 2.5 m were considered part of the matrix, which was modelled as a granular material with low, but limited cohesion. This approach created an asteroid whose interior structure is similar to its surface and whose structure overall is consistent with a gravitational collapse. For the purpose of this study, other deep interior structures are not considered.

The bulk porosity of Dimorphos results from macroporosity between individual rocks and boulders as well as microporosity within rocks. Analysis of reflectance spectra of Didymos indicates that the best meteorite analogues for boulders on Dimorphos are L/LL ordinary chondrites [20–22], which have grain densities of  $\approx 3200\text{--}3600\text{ kg/m}^3$ , and low microporosities of  $\approx 8\text{--}10\%$  [23]. Using the method described by [24] (See Dimorphos macroporosity calculations in Methods), we calculated macroporosities of  $38 \pm 3\%$  from the boulder SFD in the last complete image taken by DART [1] and  $34 \pm 4\%$  from the global SFDs measured on Dimorphos [19]. The derived macroporosity is primarily determined by the boulder SFD and the sphericity/roundness of the boulders. It is important to note that the macroporosity estimation is largely independent of the assumed minimum boulder size. In our simulations, the initial microporosity within boulders was fixed at 10% and the initial porosity of the matrix (macroporosity + microporosity) was varied between 35% and 65%. Both the porosity in the boulders and in the matrix were modelled using the  $P - \alpha$  porosity compaction model [14].

Based on laboratory measurements of meteorite falls, the average tensile strength of ordinary chondrites is  $24 \pm 11$  MPa, with no statistical difference between L and LL types [23]. In all our simulations, the initial material properties of the boulders were kept the same and we employed the tensile strength and fracture model as described in [14, 15], with parameters corresponding to a tensile strength  $Y_T \approx 20$  MPa for a  $\approx 2$  cm specimen. For the boulders on Dimorphos, the average  $Y_T \approx 10$  MPa (Table 1). However, based on previous impact studies [e.g., 18], we do not expect the impact outcome to be very sensitive to the boulder tensile strength.

The target matrix material response to shear deformation is described by a simple pressure-dependent strength model [25, 26]. The ability of a material to resist different types of stresses is an indicator of its strength. Granular materials, for instance, may exhibit considerable shear strength due to the presence of van der Waals forces and the particles’ inability to separate or slide over each other due to interlocking mechanisms [27–29]. Here we focus on the influence of the shear strength at zero pressure, commonly known as cohesion (or cohesive strength). Another important term in the strength model is the coefficient of internal friction. Though this parameter cannot be directly determined, it is possible to relate it to the angle of repose (See Methods) and bound the range of plausible values by making reasonable assumptions. The angle of repose of low cohesion materials has been measured to be  $\theta = 22^\circ$  ( $f = 0.4$ ) for glass beads [30],  $\theta = 30^\circ$  ( $f = 0.55$ ) for quartz sand [31] and  $\theta = 35\text{--}45^\circ$  ( $f = 0.7\text{--}0.9$ ) for lunar regolith [32].

On Dimorphos, for values of cohesion lower than  $Y_0 \approx 4$  Pa, the impact occurs in the gravity-dominated regime where crater growth is halted by the asteroid’s small gravity, rather than its cohesion [33]. Therefore, we first model impacts into cohesionless rubble-piles (i.e.,  $Y_0 = 0$  Pa, but with a coefficient of internal friction of  $f = 0.55$  [31], which is equivalent to  $\theta \approx 30^\circ$ ). Given our other assumptions regarding material properties, we consider that these models of impacts into targets with no cohesion provide an upper limit on the possible momentum enhancement that can be achieved from the DART impact for a given asteroid mass.

The momentum enhancement,  $\beta$ , was calculated using two distinct methods. For the first method,  $\beta$  was calculated by summing the momentum over all the SPH particles with ejection velocities larger than  $v_{esc}$ . For a given impact, the

magnitude of ejecta momentum in the direction of the net ejecta momentum is given by

$$p_{ej} = \left| \sum m_e \vec{v}_{ej} \right|, \quad (1)$$

where  $m_e$  and  $\vec{v}_{ej}$  are the mass and velocity vector of individual SPH particles, respectively. The  $p_{ej}$  calculation takes the gravitational influence of Dimorphos into account, however, it does not account for the gravitational influence of Didymos. The second method, described in [34], tracks the velocity magnitude of the asteroid centre of mass post-impact by summing the momentum of all material that remains below the escape velocity after the reaccumulation of the ejecta. The absolute difference in  $\beta$  resulting from the two calculation methods is used in the error calculation of our reported  $\beta$  values.

## Results

First, we vary the boulder volume fraction (i.e., the volume fraction of objects  $>2.5$  m in size) within the target between 0 and 50 vol%, while keeping the asteroid volume constant (Table 1). As a result, the mass and the bulk density of the asteroid vary with boulder packing. Our simulations show that  $\beta$  is relatively insensitive to the boulder volume fractions up to  $\approx 30$  vol% (Fig. 1a). For boulder volume fractions larger than about 30 vol%, the number of boulders much larger than the projectile close to the impact point is high enough that the crater efficiency and, subsequently,  $\beta$  is drastically reduced by boulder interlocking [35] and possibly armouring [36], which hinders the crater growth. These results indicate that at least the surface and shallow subsurface of Dimorphos have a low volume fraction of boulders larger than 2.5 m (less than  $\approx 40$  vol%), which is consistent with the last few images sent by DART before impact [1].

Our simulation results for the DART impact on a cohesionless surface of Dimorphos also provide a means to constrain the bulk density of the asteroid using the measured  $\beta$  (Fig. 1b), assuming a grain density in the range of 3200–3500 kg/m<sup>3</sup>. For a body with a fixed volume and grain density (Table 1), the bulk density is influenced by its porosity. The dominant effect of additional target porosity is a reduction in bulk density of the target, rather than a reduction in ejecta from compaction of pore space. For example, decreasing the bulk density of Dimorphos will increase the overall crater size and decrease the asteroid’s mass (for a fixed volume) and escape velocity. This allows for a greater total volume of ejecta to escape, but the ejecta mass is similar. Increasing the bulk density has the opposite effect. The consequence is that the total momentum of escaping ejecta measured constrains the target bulk density and porosity: for a cohesionless surface of Dimorphos, the upper bound on  $\beta$  ( $\approx 3.6$ ) implies that the bulk density of Dimorphos is less than the current best estimate of the asteroid’s bulk density of 2400 kg/m<sup>3</sup> [1]. Thus, Dimorphos is likely more porous and therefore may have a rubble-pile structure throughout the whole body.

Since the surface strength of Dimorphos is poorly constrained, for a fixed boulder distribution (30 vol%), matrix porosity ( $\phi_0 = 45\%$ ) and grain density ( $\rho_g = 3200$  and  $3500$  kg/m<sup>3</sup>) we vary the matrix material cohesion ( $Y_0 = 0$ –50 Pa) and coefficient of internal friction ( $f = 0.4$ –0.7) (See Table 1; Methods). Multiple possible combinations of cohesion, coefficient of internal friction, and bulk density could result in the observed deflection and account for the observed momentum enhancement (Fig. 1c, d). Despite this non-uniqueness, it is possible to bound the range of plausible values by making reasonable assumptions since  $f = 0.4$  is a lower limit for geological materials. For a target with  $f = 0.4$  and  $\phi_0 = 45\%$  the cohesion on the surface of Dimorphos is likely lower than  $\approx 50$  Pa (Fig. 1c, d). However, lower bulk densities ( $\rho_B < 2000$  kg/m<sup>3</sup>) or higher matrix porosities ( $\phi_0 > 55\%$ ) would require higher cohesion to match the observations (Fig. 1).

## Ejecta curtain opening angle and morphology

In our simulations of the DART impact into Dimorphos-like rubble pile targets, we observe the temporal changes of the ejecta cone opening angle and study dependences on target properties. We find no significant dependences of ejecta cone opening angle on the friction coefficient of the targets. This finding contrasts with the strong dependence of the cone opening angle on the coefficient of internal friction that is found in simulations [37] of the DART impact into

homogeneous planar targets. Our present simulations of impacts into Dimorphos-like rubble piles find that the ejecta cone opening angle and ejecta mass depend on target cohesion. In Figures 2 and 3 results for cohesionless targets ( $Y_0 = 0$  Pa) are compared with those for cohesive targets ( $Y_0 = 500$  Pa).

The ejecta plume for the cohesionless target (Fig. 2c, g) is more massive than for the cohesive target (Fig. 2d, h). For both cases, the fastest ejecta, released shortly after the impact with velocities higher than a few tens of m/s, form a cone opening angle  $\omega \approx 90^\circ$  (Fig. 3a, b). Such fast ejecta are influenced by the spacecraft geometry (e.g., [38, 39]), which is highly simplified in this study. On the other hand, slower ejecta, released at late times after the impact (hundreds to thousands of seconds) with velocities  $v_{esc} < v < 5$  m/s, form a wider ejecta cone angle of  $\approx 140^\circ$  (at 1 m/s, Fig. 3a) for the cohesionless target. For the cohesive target ( $Y_0 = 500$  Pa), crater growth ceases about 100 seconds after the impact, before the crater grows large enough for the ejection angle to be influenced by target curvature. In this case, the maximum ejecta opening angle is  $\approx 120^\circ$  (at 1 m/s, Fig. 3b). On the other hand, for the low cohesion target cases, the mass ejected at low velocities ( $v_{esc} < v < 10$  m/s) greatly exceeds the low velocity ejecta mass from the cohesive target case ( $Y_0 = 500$  Pa), implying a larger cratering efficiency and crater growth continuing to later times, and resulting in a wider cone opening angle influenced by target curvature.

The characteristics of the ejecta plume observed by LICIACube provide constraints regarding the target cohesion. At time after impact  $T = 160$  s, LICIACube’s LUKE acquired images that showed ejecta concentrated into rays which cast shadows along the ejecta cone (Fig. 2a, b). At  $T = 178$  s, the bottom of the ejecta cone and the surface of Dimorphos are obscured by the shadow cast by the ejecta (Fig. 2e,f). The shadow observed at  $T = 178$  s implies that crater growth and release of low speed ejecta continued to that time, consistent only with low cohesion target cases [e.g., 40].

Images obtained from LICIACube [4] and Hubble Space Telescope observations [5] revealed a wide ejecta cone angle, estimated to be  $\omega \approx 115\text{--}139^\circ$ . These observations determined the ejecta opening angle at specific times, up to 3 minutes after the impact for LICIACube [4] and up to 8 hr after the impact for Hubble [5]. To compare simulations results with observations of the ejecta opening angle at a specific time after impact, we determine the implied ejecta velocity at the base of the visible cone in the LICIACube images ([4]; Fig. 2e, f) using its distance above the surface and time after impact (Fig. 3).

Overall, we find that to qualitatively reproduce the amount of material observed in the ejecta cone (Fig. 2c, g), as well as the observed cone opening angle of up to  $\omega \approx 139^\circ$ , Dimorphos’ surface cohesion must not exceed  $\approx 500$  Pa. From our suite of numerical simulations with the assumed boulder packing, matrix porosity, and grain density summarised in Table 1, we find the target case with  $f = 0.55$ ,  $\rho_B = 2200$  kg/m<sup>3</sup>, and  $Y_0$  less than a few Pa is consistent with target mechanical properties inferred from surface geology [41] and produces a  $\beta$ -value (Fig. 1), excavation timescale (Fig. 2) and ejecta opening angle (Fig. 3) most consistent with observations.

## Deformation

Observations from the first few hours after impact imply that more than  $1.3\text{--}2.2 \times 10^7$  kg of ejecta were released from the DART impact (equivalent to 0.3–0.5% of Dimorphos’s mass, assuming a bulk density of 2400 kg/m<sup>3</sup>) [6]. Our simulation results for weak ( $Y_0 < 50$  Pa), Dimorphos-like targets ( $f = 0.55$  in Fig. 1c) show that the amount of ejected material could be as high as 1% of Dimorphos’ mass (Fig. 4a). At the same time, up to 8% of Dimorphos’ mass may have been displaced or ejected below the escape velocity of Dimorphos. In all impact scenarios simulated here, the DART impact does not produce a conventional impact crater and instead causes global deformation of the target (Fig. 4b).

The outcome of the impact in terms of the post-impact target morphology is highly sensitive to the target cohesion. For a cohesionless target, the ratio of the major to intermediate axes,  $a/b$ , could have changed from the reported pre-impact value of  $1.02 \pm 0.02$  [1] to as much as 1.2. Such a large change in the  $a/b$  ratio is detectable with the highest-quality post-impact lightcurve data [13, 42].

Global deformation of Dimorphos modifies the gravitational field between Didymos and Dimorphos and leads to significant implications for its orbit. The shape change would cause an additional perturbation to Dimorphos’s orbit, on top of those caused by the spacecraft momentum and ejecta recoil, and this effect can account for a few seconds to

several minutes of the observed orbit period change (i.e.,  $\sim 33$  minutes), depending on the magnitude of the deformation [43]. Any deformation would alter Dimorphos’s mass distribution and affect its post-impact rotation state (e.g., [44, 45]).

### Implications for binary asteroid system formation

Our numerical simulations suggest that Dimorphos is likely a rubble-pile asteroid with a bulk density comparable to or lower than that of Didymos. Our calculations based on the observed boulder SFD indicate that the macroporosity estimate for the surface of Dimorphos ( $\approx 35\%$ ) is approximately twice the value obtained for the surface of Ryugu, as determined through the same method [24, 46], but comparable with the macroporosity on Itokawa [24, 47]. However, it is worth noting that this estimate is only a rough approximation due to the limited data currently available and the upcoming Hera mission will be able to provide better constraints.

Our findings serve as crucial evidence regarding the origin of Dimorphos as a secondary in a double asteroid system. To maintain its structural stability given its rapid rotation period of 2.26 hours, the primary, Didymos, likely requires a higher cohesive strength, estimated to be on the order of 10s Pa [48]. This level of cohesion can be attributed to van der Waals forces acting between the fine regolith grains [49], or to a coherent inner core [50]. However, our best-fit scenarios indicate that Dimorphos, the satellite of Didymos, exhibits a cohesive strength of less than a few Pa. This observed disparity in cohesive strength between Didymos and Dimorphos suggests a potential scarcity of fine grains within Dimorphos’ structure as well as a weak and fragmented internal structure.

The material properties estimated in our study support the hypothesis that Dimorphos formed through rotationally or impact-induced mass shedding and subsequent re-accumulation from Didymos. The accretion of orbiting mass shed from Didymos occurs over a period of several days to years [51], during which fine grains tend to escape from the system due to solar radiation pressure [52]. As a result, the accreted satellite, Dimorphos, has limited fines and cohesion.

While the mechanical properties of Dimorphos resemble those of Ryugu and Bennu (e.g., [17, 53–55]), these findings may not be applicable to single small S-type asteroids, specifically to their moons. The implications of our study may extend beyond Dimorphos and provide valuable insights into the formation processes of similar small S-type binary asteroid systems.

Moreover, since the DART spacecraft likely caused global deformation of Dimorphos, we can infer that similarly formed asteroid moons are easily reshaped and their surfaces are relatively young [16]. Overall, the findings of this study provide valuable information for understanding the formation and characteristics of binary asteroids, and will inform future exploration and asteroid deflection efforts.

## Data Availability

Additional supporting information and input data for the model simulations used in this work is archived on GitHub (doi:10.5281/zenodo.10246671).

## Code availability

A compiled version of the Bern SPH code, as well as the necessary input files are available from the corresponding author upon request. SPH data visualisation was produced using the NCAR Visualization and Analysis Platform for Ocean, Atmosphere, and Solar Researchers (VAPOR version 3.8.0) [Software] (doi:10.5281/zenodo.7779648).

## Acknowledgments

We thank Jessica Sunshine, Mallory DeCoster, Dawn Graninger, Jason Pearl, Angela Stickle and the rest of the DART Impact Working Group for the constructive discussions.

SDR and MJ acknowledge support by the Swiss National Science Foundation (project number 200021\_207359). This work was supported by the DART mission, NASA Contract No. 80MSFC20D0004. GSC and TMD acknowledge support from UK Science and Technology Facilities Council Grant ST/S000615/1. FF acknowledges funding from the Swiss National Science Foundation (SNSF) Ambizione grant No. 193346. KMK, MBS, JMO Portions of this work were performed by Lawrence Livermore National Laboratory under DOE Contract DE-AC52-07NA27344. LLNL-JRNL-846795, PM acknowledges financial support from the CNRS through the MITI interdisciplinary programs through its exploratory research program an, from ESA and from the University of Tokyo. PM, RL, KW, NM and CQR acknowledge the support from the European Union's Horizon 2020 research and innovation program, grant agreement No. 870377 (project NEO-MAPP). NM, CQR and PM acknowledge funding support from the Centre National d'Etudes Spatiales (CNES). RN acknowledges support from NASA/FINESST (NNH20ZDA001N/80NSSC21K1527). ED, EME, PHH, SI, AL, MP, AR and FT acknowledge financial support from Agenzia Spaziale Italiana (ASI, contract No. 2019-31-HH.0). MP, AL and FT also acknowledge support from ASI, contract No. 2022-8-HH.0. Work by EGF was carried out at the Jet Propulsion Laboratory, California Institute of Technology, under a contract with the National Aeronautics and Space Administration (#80NM0018D0004). JO acknowledge support by grant PID2021-125883NB-C22 by the Spanish Ministry of Science and Innovation/State Agency of Research MCIN/AEI/ 10.13039/501100011033 and by 'ERDF A way of making Europe'. JO, IH, SR, MJ, RL, KW acknowledge support by Consejo Superior de Investigaciones Científicas (CSIC) (project ILINK22061). The work by PP was supported by the Grant Agency of the Czech Republic, grant 20-04431S.

## Author contributions

SDR, MJ, AFC conceptualised the study. SDR ran the simulations and analysed the data. SDR, MJ, AFC, OB, GSC wrote the initial draft. YZ provided rubble-pile models. RTD, CME, OB provided the shape model of Dimorphos. TLF provided the viewing geometry for comparison to LICIACube data. MH, JYL, PHH provided measurements of the ejecta. YZ, FF, HFA helped with the interpretation of results. RN helped with the deformation affects on dynamics. MP, AL, FT provided boulder SFDs. CQR, NM provided the boulder shapes. AFC, HFA, BWB provided momentum enhancement measurements. AR, ED, PHH provided LICIACube measurements. PP provided observational inputs. PS helped with the interpretation of cohesion. TMD, KMK, PM, MBS, NLC, ED, EGF, IH, SI, RL, JO, MO, ASR, KW, AZ, EME provided comments that substantively revised the manuscript. CM, BHM provided the stereographs of the Didymos system.

## Competing interests

The authors declare no competing interests

## Tables

Table 1: Table of fixed and varied target parameters.

Fixed parameters	
Target dimensions [1]	$177 \times 174 \times 116$ m
Target volume [1]	$0.00181$ km <sup>3</sup>
Boulders SFD [19]	see Methods
Boulders at impact location [1]	see Methods
Boulder tensile strength	10 MPa
Boulder porosity	10%
Varied parameters	
Boulder packing	0 – 50 vol%
Grain density, $\rho_g$	3200/3500 kg/m <sup>3</sup>
Matrix porosity, $\phi_0$	35 – 65%
Matrix cohesion, $Y_0$	0 – 500 Pa
Matrix internal friction coeff., $f$	0.4 – 0.7

## Figure Legends/Captions



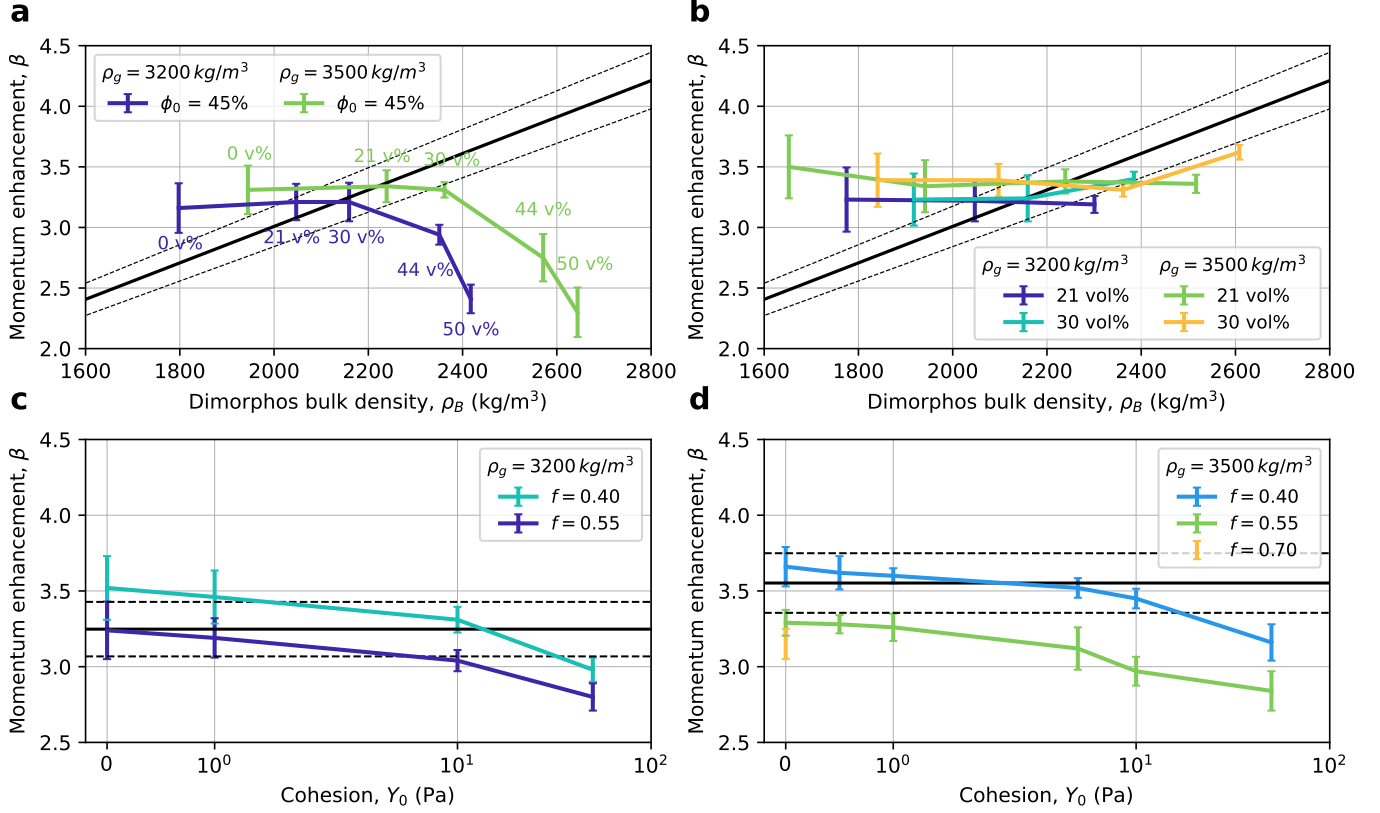


Figure 1: Momentum enhancement,  $\beta$ , as derived from SPH simulations. The continuous black lines show the  $\beta$  dependence on Dimorphos' bulk density,  $\rho_B$ , derived from dynamical simulations [7] ( $1\text{-}\sigma$  uncertainty is shown by the dashed lines). Data points that cross the solid black line are consistent with the measured  $\beta$  from the DART impact. The uncertainty on each simulation data (vertical bars) is calculated from the absolute difference in  $\beta$  calculated from two different methods (see Momentum enhancement calculations; Methods). (a)  $\beta$  as a function of  $\rho_B$ , for cohesionless targets with the same dimensions as Dimorphos [1] and with boulder volume fractions ranging from 0 vol% (no boulders larger than 2.5 m) to 50 vol%. For fixed target volume ( $0.00181 \text{ km}^3$ ) and fixed matrix porosity ( $\phi_0 = 45\%$ ), the mass and bulk density of Dimorphos vary with boulder packing. (b)  $\beta$  as a function of  $\rho_B$  for cohesionless targets with varying matrix porosity, between 35 and 65% and two boulder packings: 21 and 30 vol%.  $\rho_B$  is calculated for a fixed asteroid volume and it varies with matrix porosity and boulder packing. (c)  $\beta$  as a function of matrix cohesion ( $Y_0$ ) for the DART impact into targets with varying coefficient of internal friction ( $f = 0.4\text{--}0.55$ ), an assumed grain density,  $\rho_g = 3200 \text{ kg/m}^3$  and a 30 vol% boulder packing. The horizontal line shows the  $\beta$  derived from dynamical simulations for a target with  $\rho_B = 2160 \text{ kg/m}^3$  (minimum density consistent with 1a and 1b results). (d)  $\beta$  as a function of  $Y_0$  for the DART impact into targets with  $f = 0.4\text{--}0.70$ ,  $\rho_g = 3500 \text{ kg/m}^3$  and 30 vol% boulder packing. The horizontal line shows the  $\beta$  derived from dynamical simulations for a target with  $\rho_B = 2360 \text{ kg/m}^3$  (maximum density consistent with 1a and 1b results).

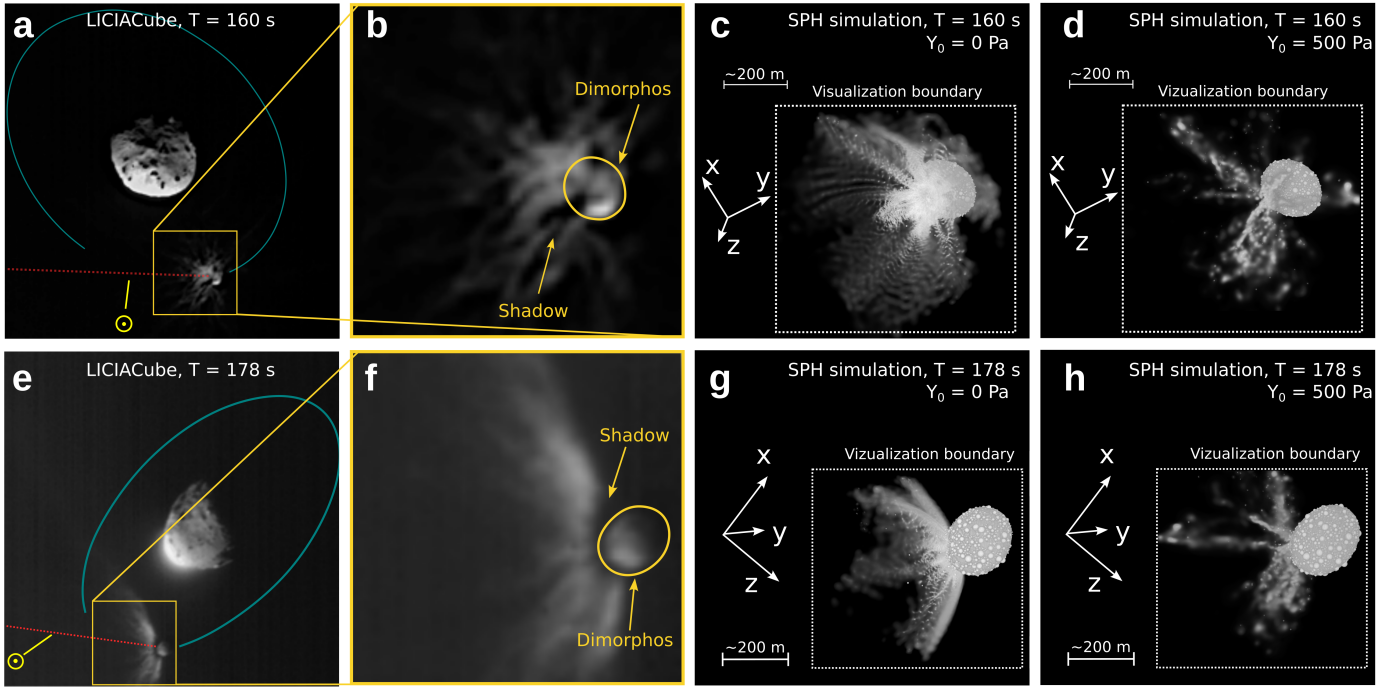


Figure 2: LICIACube images of the expanding ejecta cone adapted from [4] compared with SPH simulation results. (a) Image acquired by the LUKE instrument onboard LICIACube at a distance of  $\approx 76$  km, 160 seconds after the impact. (b) Zoomed-in image of Dimorphos and impact ejecta. The approximate outline of the asteroid is shown in yellow. The ejecta curtain exhibits undulations, filamentary patterns, and shadows. (c) Bern SPH simulation of the DART impact into a cohesionless, rubble-pile Dimorphos-sized target (with  $f = 0.55$  and  $\phi_0 = 45\%$ ), at  $T = 160$  s. Due to the limited visualisation domain, only a portion of the ejecta are shown. (d) Simulation of the impact into a rubble-pile Dimorphos-sized target with  $Y_0 = 500$  Pa ( $\beta = 2.26 \pm 0.28$ ). (e) Image acquired by LUKE at a distance of  $\approx 71$  km, 178 seconds after the impact. (f) Zoomed-in image of Dimorphos and impact ejecta. (g) Same as (c) but at  $T = 178$  s. (h) Same as (d) but at  $T = 178$  s. The optical depth of the ejecta cone is not computed for this comparison between the observations and simulations output.

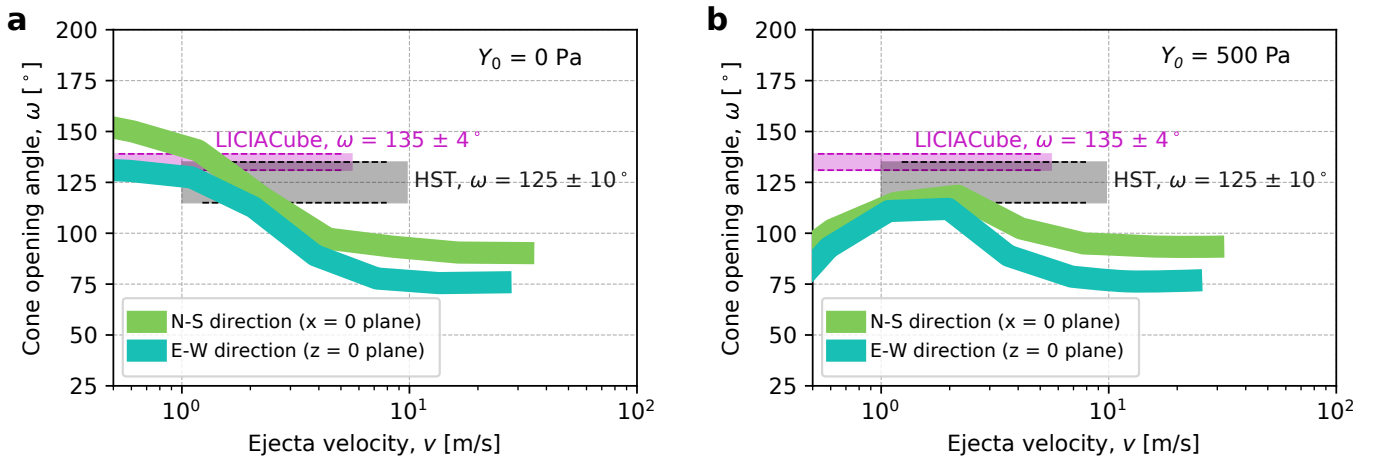


Figure 3: Ejecta cone opening angle. (a) Cone opening angle derived from cohesionless ( $Y_0 = 0$  Pa) SPH simulations (shown in Fig. 2c and g) in the N-S direction ( $x = 0$  plane) and in the E-W direction ( $z = 0$  plane). (b) Cone opening angle derived from SPH simulations with  $Y_0 = 500$  Pa in the N-S direction ( $x = 0$  plane) and in the E-W direction ( $z = 0$  plane). In both (a) and (b) the cone opening angle derived from observations is plotted for comparison:  $\omega = 135 \pm 4^\circ$  is measured from LICIACube data based on the opening angle at the base of the cone at  $T \approx 170$  s, resulting in ejecta velocities in the range of a few cm/s – a few tens cm/s [4] and  $\omega = 125 \pm 10^\circ$  is measured in the Hubble Space Telescope (HST) data for ejecta in the range of 1–10 m/s [5]. Temporal evolution measurements of the observed ejecta cone is not possible due to the limited observation window.

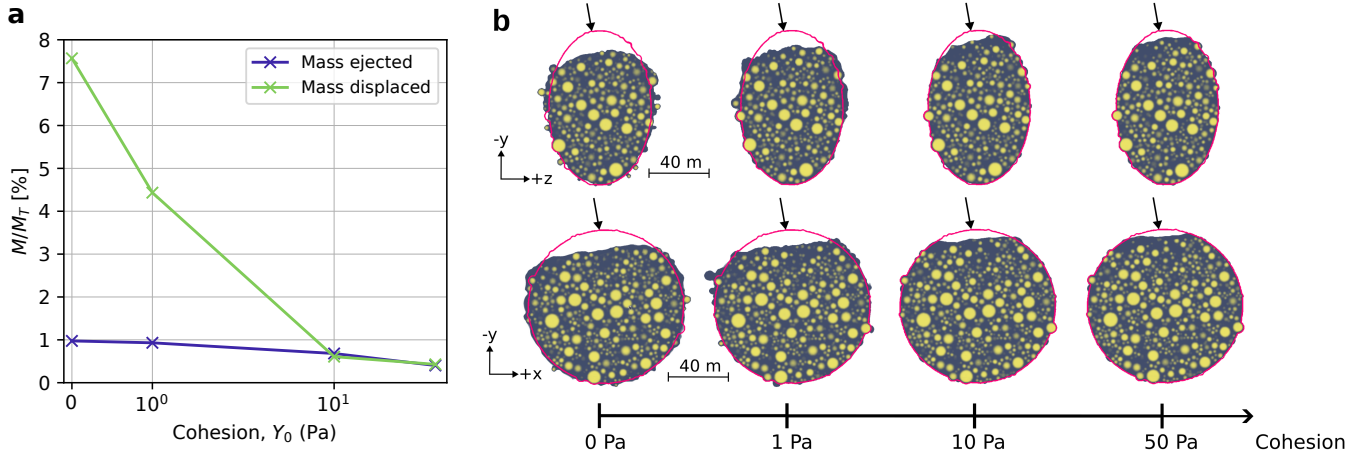


Figure 4: Global deformation of Dimorphos. (a) Total target mass ejected with speeds above  $v_{esc}$  and total target mass displaced or ejected below  $v_{esc}$ , normalised by the initial target mass,  $M_T$ , for a Dimorphos-like target with  $f = 0.55$ ,  $\phi_0 = 45\%$  and cohesion levels between  $Y_0$  0 and 50 Pa. (b) Two-dimensional slices (taken at  $x = 0$  in the  $y - z$  plane and at  $z = 0$  in the  $x - y$  plane), at  $T \approx 1$  hour after the impact. The boulder material is shown in yellow and the matrix material is shown in blue. The red contour shows the initial target profile, before the impact. The black arrows show the impact direction.

## References

1. Daly, R. T. *et al.* Successful Kinetic Impact into an Asteroid for Planetary Defense. *Nature*, 1–3. ISSN: 1476-4687 (2023).
2. Thomas, C. A. *et al.* Orbital Period Change of Dimorphos Due to the DART Kinetic Impact. *Nature*, 1–3. ISSN: 1476-4687 (2023).
3. Dotto, E. *et al.* LICIACube - The Light Italian Cubesat for Imaging of Asteroids In support of the NASA DART mission towards asteroid (65803) Didymos. *Planetary and Space Science* **199**, 105185. ISSN: 0032-0633 (2021).
4. Dotto, E. *et al.* The Dimorphos ejecta plume properties revealed by LICIACube. *Nature*, 1–5. (2024) (2024).
5. Li, J.-Y. *et al.* Ejecta from the DART-produced active asteroid Dimorphos. *Nature*, 1–3. ISSN: 1476-4687 (2023).
6. Graykowski, A. *et al.* Light Curves and Colors of the Ejecta from Dimorphos after the DART Impact. *Nature*, 1–3 (2023).
7. Cheng, A. F. *et al.* Momentum Transfer from the DART Mission Kinetic Impact on Asteroid Dimorphos. *Nature*, 1–3. ISSN: 1476-4687 (2023).
8. Michel, P. *et al.* The ESA Hera Mission: Detailed Characterization of the DART Impact Outcome and of the Binary Asteroid (65803) Didymos. *The Planetary Science Journal* **3**, 160 (2022).
9. Rivkin, A. S. *et al.* The Double Asteroid Redirection Test (DART): Planetary Defense Investigations and Requirements. *Planetary Science Journal* (2021).
10. Holsapple, K. A. & Housen, K. R. Momentum transfer in asteroid impacts. I. Theory and scaling. *Icarus* **221**, 875–887. ISSN: 0019-1035 (2012).
11. Raducan, S. D., Davison, T. M., Luther, R. & Collins, G. S. The role of asteroid strength, porosity and internal friction in impact momentum transfer. *Icarus* **329**, 282–295. ISSN: 0019-1035 (2019).
12. Stickle, A. M. *et al.* Effects of Impact and Target Parameters on the Results of a Kinetic Impactor: Predictions for the Double Asteroid Redirection Test (DART) Mission. *The Planetary Science Journal* **3**, 248. ISSN: 2632-3338 (2022).
13. Pravec, P. *et al.* Photometric Observations of the Binary Near-Earth Asteroid (65803) Didymos in 2015–2021 Prior to DART Impact. *The Planetary Science Journal* **3**, 175. ISSN: 2632-3338 (2022).
14. Jutzi, M., Benz, W. & Michel, P. Numerical simulations of impacts involving porous bodies: I. Implementing sub-resolution porosity in a 3D SPH Hydrocode. *Icarus* **198**, 242–255. ISSN: 00191035 (Nov. 2008).
15. Jutzi, M. SPH calculations of asteroid disruptions: The role of pressure dependent failure models. *Planet. Space Sci* **107**, 3–9. ISSN: 0032-0633 (2015).
16. Raducan, S. D. & Jutzi, M. Global-scale Reshaping and Resurfacing of Asteroids by Small-scale Impacts, with Applications to the DART and Hera Missions. en. *The Planetary Science Journal* **3**, 128. ISSN: 2632-3338. (2022) (June 2022).
17. Jutzi, M., Raducan, S. D., Zhang, Y., Michel, P. & Arakawa, M. Constraining surface properties of asteroid (162173) Ryugu from numerical simulations of Hayabusa2 mission impact experiment. *Nature Communications* **13**, 7134 (2022).
18. Ormö, J. *et al.* Boulder exhumation and segregation by impacts on rubble-pile asteroids. *Earth and Planetary Science Letters* **594**, 117713. ISSN: 0012-821X (2022).
19. Pajola, M. *et al.* The boulder size-frequency distribution derived from DART/DRACO images of Dimorphos: First results. *54th Lunar and Planetary Science Conference* (2023).

20. De León, J., Licandro, J., Duffard, R. & Serra-Ricart, M. Spectral analysis and mineralogical characterization of 11 olivine–pyroxene rich NEAs. *Advances in Space Research. The Moon and Near-Earth Objects* **37**, 178–183. ISSN: 0273-1177 (Jan. 2006).
21. Dunn, T. L., Burbine, T. H., Bottke, W. F. & Clark, J. P. Mineralogies and source regions of near-Earth asteroids. *Icarus* **222**, 273–282. ISSN: 0019-1035 (2013).
22. Ieva, S. *et al.* Spectral Rotational Characterization of the Didymos System prior to the DART Impact\*. *The Planetary Science Journal* **3**. Publisher: IOP Publishing, 183. ISSN: 2632-3338 (2022).
23. Flynn, G. J., Consolmagno, G. J., Brown, P. & Macke, R. J. Physical properties of the stone meteorites: Implications for the properties of their parent bodies. *Geochemistry* **78**, 269–298. ISSN: 0009-2819 (2018).
24. Grott, M. *et al.* Macroporosity and Grain Density of Rubble Pile Asteroid (162173) Ryugu. *Journal of Geophysical Research: Planets* **125**, e2020JE006519 (2020).
25. Lundborg, N. The strength-size relation of granite. *International Journal of Rock Mechanics and Mining Sciences & Geomechanics Abstracts* **4**, 269–272. ISSN: 0148-9062 (1967).
26. Collins, G. S., Melosh, H. J. & Ivanov, B. A. Modeling damage and deformation in impact simulations. *Meteoritics & Planetary Science* **39**, 217–231. ISSN: 1945-5100 (2004).
27. Sánchez, P. & Scheeres, D. J. The strength of regolith and rubble pile asteroids. *Meteoritics & Planetary Science* **49**, 788–811 (2014).
28. Scheeres, D. J. *et al.* The dynamic geophysical environment of (101955) Bennu based on OSIRIS-REx measurements. *Nature Astronomy* **3**, 352–361 (2019).
29. Ferrari, F. & Tanga, P. The role of fragment shapes in the simulations of asteroids as gravitational aggregates. *Icarus* **350**, 113871. ISSN: 0019-1035 (2020).
30. Lajeunesse, E., Monnier, J. B. & Homsy, G. M. Granular slumping on a horizontal surface. *Physics of Fluids* **17**, 103302. ISSN: 1070-6631 (2005).
31. Lube, G., Huppert, H. E., Sparks, R. S. J. & Hallworth, M. A. Axisymmetric collapses of granular columns. *Journal of Fluid Mechanics* **508**, 175–199. ISSN: 1469-7645, 0022-1120 (2004).
32. Mitchell, J. K. *et al.* Mechanical properties of lunar soil: Density, porosity, cohesion and angle of internal friction. *Lunar and Planetary Science Conference Proceedings* **3**, 3235 (Jan. 1972).
33. Cheng, A. F. *et al.* Model of Double Asteroid Redirection Test Impact Ejecta Plume Observations. *The Planetary Science Journal* **3**, 131. ISSN: 2632-3338 (2022).
34. Bruck Syal, M., Michael Owen, J. & Miller, P. L. Deflection by kinetic impact: Sensitivity to asteroid properties. *Icarus* **269**, 50–61 (2016).
35. Raducan, S. D., Jutzi, M., Zhang, Y., Ormö, J. & Michel, P. Reshaping and ejection processes on rubble-pile asteroids from impacts. *Astronomy & Astrophysics* **665**, L10 (2022).
36. Tatsumi, E. & Sugita, S. Cratering efficiency on coarse-grain targets: Implications for the dynamical evolution of asteroid 25143 Itokawa. *Icarus* **300**, 227–248 (Jan. 2018).
37. Raducan, S. D., Davison, T. M. & Collins, G. S. Ejecta distribution and momentum transfer from oblique impacts on asteroid surfaces. *Icarus* **374**, 114793. ISSN: 0019-1035 (2022).
38. Raducan, S. D. *et al.* Influence of the projectile geometry on the momentum transfer from a kinetic impactor and implications for the DART mission. *International Journal of Impact Engineering* **162**, 104147. ISSN: 0734-743X (2022).
39. Owen, J. M., DeCoster, M. E., Graninger, D. M. & Raducan, S. D. Spacecraft Geometry Effects on Kinetic Impactor Missions. *The Planetary Science Journal* **3**, 218. ISSN: 2632-3338 (2022).

40. Holsapple, K. A. & Housen, K. R. A crater and its ejecta: An interpretation of Deep Impact. *Icarus. Deep Impact at Comet Tempel 1* **191**, 586–597. ISSN: 0019-1035 (2007).
41. Ernst, C. M. *et al.* CHARACTERIZATION OF THE DART IMPACT SITE ON Dimorphos. *54th Lunar and Planetary Science Conference* (2023).
42. Pravec, P. *et al.* Binary asteroid population. 3. Secondary rotations and elongations. *Icarus* **267**, 267–295. ISSN: 0019-1035 (2016).
43. Nakano, R. *et al.* NASA’s Double Asteroid Redirection Test (DART): Mutual Orbital Period Change Due to Reshaping in the Near-Earth Binary Asteroid System (65803) Didymos. *The Planetary Science Journal* **3**, 148. ISSN: 2632-3338 (2022).
44. Agrusa, H. F. *et al.* The excited spin state of Dimorphos resulting from the DART impact. *Icarus* **370**, 114624. ISSN: 0019-1035 (2021).
45. Richardson, D. C. *et al.* Predictions for the Dynamical States of the Didymos System before and after the Planned DART Impact. *The Planetary Science Journal* **3**, 157. ISSN: 2632-3338 (2022).
46. Tricarico, P. *et al.* Internal rubble properties of asteroid (101955) Bennu. *Icarus* **370**, 114665. ISSN: 0019-1035 (2021).
47. Fujiwara, A. *et al.* The Rubble-Pile Asteroid Itokawa as Observed by Hayabusa. *Science* **312**, 1330–1334 (2006).
48. Zhang, Y. *et al.* Creep stability of the DART/Hera mission target 65803 Didymos: II. The role of cohesion. *Icarus* **362**, 114433 (2021).
49. Scheeres, D. J., Hartzell, C. M., Sanchez, P. & Swift, M. Scaling forces to asteroid surfaces: The role of cohesion. *Icarus* **210**, 968–984 (2010).
50. Ferrari, F. & Tanga, P. Interior of top-shaped asteroids with cohesionless surface. *Icarus* **378**, 114914 (May 2022).
51. Walsh, K. J., Richardson, D. C. & Michel, P. Rotational breakup as the origin of small binary asteroids. *Nature* **454**, 188–191 (2008).
52. Ferrari, F., Raducan, S. D., Soldini, S. & Jutzi, M. Ejecta Formation, Early Collisional Processes, and Dynamical Evolution after the DART Impact on Dimorphos. *The Planetary Science Journal* **3**, 177 (2022).
53. Arakawa, M. *et al.* An artificial impact on the asteroid (162173) Ryugu formed a crater in the gravity-dominated regime. *Science* **368**, 67–71. ISSN: 0036-8075 (2020).
54. Walsh, K. J. *et al.* Near-zero cohesion and loose packing of Bennu’s near subsurface revealed by spacecraft contact. *Science Advances* **8**, eabm6229 (2022).
55. Barnouin, O. S. *et al.* The Formation of Terraces on Asteroid (101955) Bennu. *Journal of Geophysical Research: Planets* **127**, e2021JE006927. ISSN: 2169-9100 (2022).